

# **Ni-O-Ag catalyst enables 103-m<sup>2</sup> artificial photosynthesis with >16% solar-to-chemical energy conversion efficiency**

Yaguang Li<sup>1,4,\*</sup>, Fanqi Meng<sup>2,4</sup>, Qixuan Wu<sup>1,4</sup>, Dachao Yuan<sup>3,4</sup>, Haixiao Wang<sup>1</sup>, Bang Liu<sup>1</sup>, Junwei Wang<sup>1</sup>, Xingyuan San<sup>1</sup>, Lin Gu<sup>2</sup>, Shufang Wang<sup>1</sup>, Qingbo Meng<sup>2,\*</sup>

<sup>1</sup>Research Center for Solar Driven Carbon Neutrality, The College of Physics Science and Technology, Institute of Life Science and Green Development, Hebei University, Baoding, 071002, China.

<sup>2</sup>Beijing National Laboratory for Condensed Matter Physics, Institute of Physics, Chinese Academy of Sciences, Beijing, 100190, China.

<sup>3</sup>College of Mechanical and Electrical Engineering, Hebei Agricultural University, Baoding 071001, China.

<sup>4</sup>These authors contributed equally to this work.

Correspondence and requests for materials should be addressed to Y. Li. (email: liyaguang@hbu.edu.cn) or to Q. Meng. (email: qbmeng@iphy.ac.cn).

## Abstract

Herein, NiO nanosheets supported with Ag single atoms (2D Ni<sub>1</sub>Ag<sub>0.02</sub>O<sub>1</sub>) are synthesized for photothermal CO<sub>2</sub> hydrogenation to achieve 1065 mmol g<sup>-1</sup> h<sup>-1</sup> of CO production rate under 1 sun irradiation, revealing the unparalleled weak sunlight driven reverse water-gas shift reaction (RWGS) activity. This performance is attributed to the coupling effect of Ag-O-Ni sites to enhance the hydrogenation of CO<sub>2</sub> and weaken the CO adsorption, resulting in 1434 mmol g<sup>-1</sup> h<sup>-1</sup> of CO yield at 300 °C, surpassing any low-temperature RWGS performances ever reported. Building on this, we integrated the 2D Ni<sub>1</sub>Ag<sub>0.02</sub>O<sub>1</sub> supported photothermal RWGS with commercial photovoltaic electrolytic water splitting, leading to the realization of 103-m<sup>2</sup> scale artificial photosynthesis system (CO<sub>2</sub>+H<sub>2</sub>O→CO+H<sub>2</sub>O) with a daily CO yield of 18.70 m<sup>3</sup>, a photochemical energy conversion efficiency of >16%, over 90% H<sub>2</sub> utilization efficiency, outperforming other types of artificial photosynthesis. The results of this research chart a promising course for designing practical, natural sunlight-driven artificial photosynthesis systems and highly efficient platinum-free CO<sub>2</sub> hydrogenation catalysts. This work is a significant step towards harnessing solar energy more efficiently and sustainably, opening exciting possibilities for future research and development in this area.

## Introduction

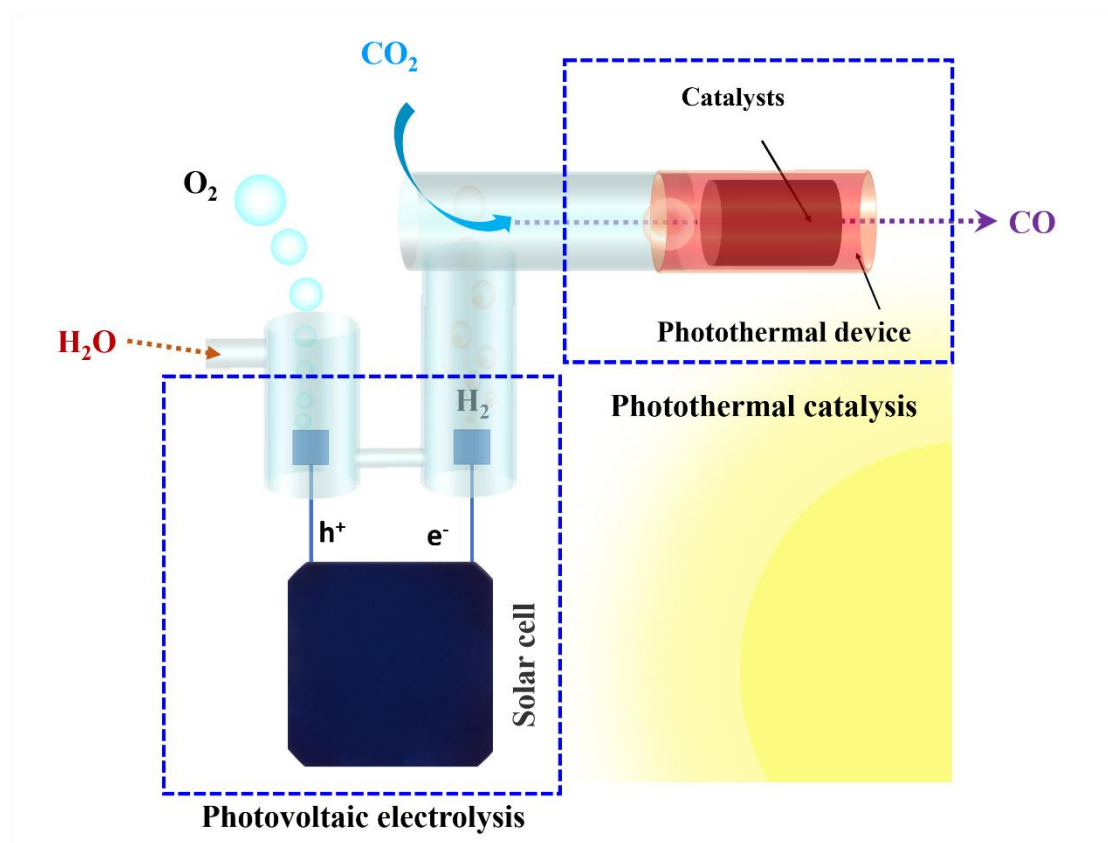
Artificial photosynthesis, which uses solar energy to convert CO<sub>2</sub> into chemicals and fuels, is emerging as a promising path towards carbon neutrality.<sup>1,2</sup> Given that carbon monoxide (CO) is a vital precursor for many valuable fuels and chemicals in various industries,<sup>3,4</sup> numerous artificial photosynthetic systems have been developed for solar driven CO generation by using CO<sub>2</sub> and H<sub>2</sub>O (CO<sub>2</sub>+H<sub>2</sub>O→CO+O<sub>2</sub>).<sup>5,6</sup> With the development of various efficient catalysts, such as metals,<sup>7-9</sup> metal compounds,<sup>10-12</sup> molecular complexes,<sup>13,14</sup> the size and solar to chemical energy efficiency (STC) of artificial photosynthetic systems have made great progress (for example, the device with 6.5 m<sup>2</sup> size, 3.8% STC<sup>15</sup> and the device with 1 cm<sup>2</sup> size and 12.7% STC<sup>16</sup>), revealing the dawn of applicable artificial photosynthesis. However, the state of the art of STC and scale level are still far from meeting practical needs. Therefore, it is one of the holy grails for scientists to synergistically further improve the STC and scale of artificial photosynthesis.

Recognizing that artificial photosynthesis comprises two main processes of water splitting and CO<sub>2</sub> hydrogenation,<sup>17,18</sup> a novel artificial photosynthesis paradigm has been suggested: the integration of photovoltaic-electrolytic water splitting and photothermal CO<sub>2</sub> hydrogenation (Scheme 1),<sup>19</sup> with ability for large-scale implementation. However, for practical applications, these systems need to operate under ambient conditions. While photovoltaic-electrolytic water splitting can already work under natural sunlight irradiation, the photothermal reverse water-gas shift reaction (RWGS, CO<sub>2</sub>+H<sub>2</sub>→CO+H<sub>2</sub>O) necessitates high brightness sunlight irradiation (light intensity > 10 kW m<sup>-2</sup> = 10 suns) to create high temperature (>450 °C) to maintain operation.<sup>20,21</sup>

Consequently, such systems are unable to function outdoors under typical sunlight conditions using standard photothermal configurations. To address this challenge, in addition to increasing the ambient sunlight driven temperature, the key is to decrease the reaction temperature of RWGS. This has led scientists to develop catalysts based on platinum-group metals that are highly active for RWGS at low temperatures.<sup>22-25</sup> For instance, Ma et al. reported a Pt-MoO<sub>x</sub>/Mo<sub>2</sub>N catalyst that achieves a RWGS CO generation rate of 619.2 mmol g<sup>-1</sup> h<sup>-1</sup> at 300 °C.<sup>26</sup> Despite these advances, platinum-group-metal-based catalysts have not yet demonstrated functionality under ambient sunlight and the use of platinum group metals (Pt, Rh, Ru, Pd) significantly increase their cost. Consequently, developing platinum-group-metals free RWGS catalysts with excellent low-temperature activity (<300 °C) and low cost is crucial for realizing efficient ambient sunlight driven photothermal RWGS.

In this study, we designed a catalyst that loaded Ag single atoms on NiO support (2D Ni<sub>1</sub>Ag<sub>0.02</sub>O<sub>1</sub>) for low-temperature RWGS to show a CO yield of 418.95 mmol g<sup>-1</sup> h<sup>-1</sup> and 1434 mmol g<sup>-1</sup> h<sup>-1</sup> at 250 °C and 300 °C, respectively, exceeding to any previously reported counterparts. Characterizations and theoretical calculations revealed that the Ag-O-Ni synergistic sites facilitated asymmetric activation of CO<sub>2</sub> and the weak adsorption of CO, thus enhancing the RWGS activity. This low-temperature catalytic performance enabled 2D Ni<sub>1</sub>Ag<sub>0.02</sub>O<sub>1</sub> to realize efficient weak sunlight driven photothermal RWGS, with a CO production rate of 1065 mmol g<sup>-1</sup> h<sup>-1</sup> under 1 sun illumination. Owing to its ability to operate efficiently under weak sunlight irradiation, 2D Ni<sub>1</sub>Ag<sub>0.02</sub>O<sub>1</sub> assisted photothermal RWGS could be paired with photovoltaic

electrolytic H<sub>2</sub>O decomposition to convert CO<sub>2</sub> and H<sub>2</sub>O into CO and O<sub>2</sub> under outdoor sunlight irradiation with a scale of 103 m<sup>2</sup> and a STC of >16% throughout the daytime, paving a new benchmark for large-sized artificial photosynthesis.



**Scheme 1.** Schematic map of artificial photosynthesis composed by photovoltaic electrolytic water splitting and photothermal CO<sub>2</sub> hydrogenation.

## Results and discussions

### Ag single atoms supported on NiO

In a typical synthesis process, we added Ni(NO<sub>3</sub>)<sub>3</sub>·6H<sub>2</sub>O, AgNO<sub>3</sub> and water-soluble starch into the water to form a homogeneous solution. And the solution was frozen with liquid nitrogen and removed the water by lyophilization. Then, an annealing process in

the air was applied to form the catalyst (synthesis details are seen in Methods). Fig. 1a, b present the typical scanning electron microscopy (SEM) and transmission electron microscopy (TEM) images of the as-prepared catalyst. The catalyst was grown in two-dimensional morphology and no clear Ag nanoparticles existed in the visual field. Powder X-ray diffraction (XRD) pattern showed that the catalyst had only peaks assigned to NiO rather than Ag based species (Supplementary Fig. 1).<sup>27</sup> The high resolution (HRTEM) image of the catalyst revealed typical NiO(111) crystal planes with the identical lattice spacing of 0.242 nm (Fig. 1c)<sup>28</sup>, while X-ray photoelectron spectroscopy (XPS) also confirmed the oxidation state of Ni (Supplementary Fig. 2).<sup>29</sup> Further, elemental mapping images demonstrated the homogeneous distribution of O, Ni and Ag, throughout the sample (Fig. 1d), confirming the existence of Ag species. To visualize the Ag species, high angle annular dark-field scanning TEM (HAADF-STEM) was applied and Fig. 1e revealed numerous star-like bright spots on the surface of the sample, which were assigned to Ag single atoms.<sup>30</sup> The atomic ratio of Ag in the sample was 2%. Therefore, we named the catalyst as 2D Ni<sub>1</sub>Ag<sub>0.02</sub>O<sub>1</sub>. Atomic force microscopy (AFM) confirmed that the thickness of 2D Ni<sub>1</sub>Ag<sub>0.02</sub>O<sub>1</sub> was 4 nm, revealing its ultrathin nature (Fig. 1f). We used the X-ray absorption spectroscopy (XAS) to characterize the coordination structure of Ag in 2D Ni<sub>1</sub>Ag<sub>0.02</sub>O<sub>1</sub>. As shown in Fig. 1g, the energy of Ag K-edge in 2D Ni<sub>1</sub>Ag<sub>0.02</sub>O<sub>1</sub> was higher than that of Ag foil and lower than that of Ag<sub>2</sub>O.<sup>31</sup> It indicated that the Ag single atoms in 2D Ni<sub>1</sub>Ag<sub>0.02</sub>O<sub>1</sub> slightly oxidation (Supplementary Fig. 3).<sup>32</sup> Fourier transformed EXAFS (FTEXAFS) of 2D Ni<sub>1</sub>Ag<sub>0.02</sub>O<sub>1</sub> showed a peak located at 1.6 Å, corresponding to the Ag-O coordination (Fig. 1h).

Moreover, FTEXAFS showed no other peaks for 2D  $\text{Ni}_1\text{Ag}_{0.02}\text{O}_1$ ,<sup>33</sup> confirming the single atomic state of Ag. Computational simulation identified that the Ag-O coordination number of Ag in 2D  $\text{Ni}_1\text{Ag}_{0.02}\text{O}_1$  was 1 (Supplementary Table 1).<sup>34</sup> Based on the EXAFS results, we built the atomic structure of 2D  $\text{Ni}_1\text{Ag}_{0.02}\text{O}_1$ . As shown in Fig. 1i, the Ag single atom was bonded to the lattice oxygen of NiO support, which aligned well with the experimentally obtained FT-EXAFS curve of 2D  $\text{Ni}_1\text{Ag}_{0.02}\text{O}_1$  (Fig. 1i).

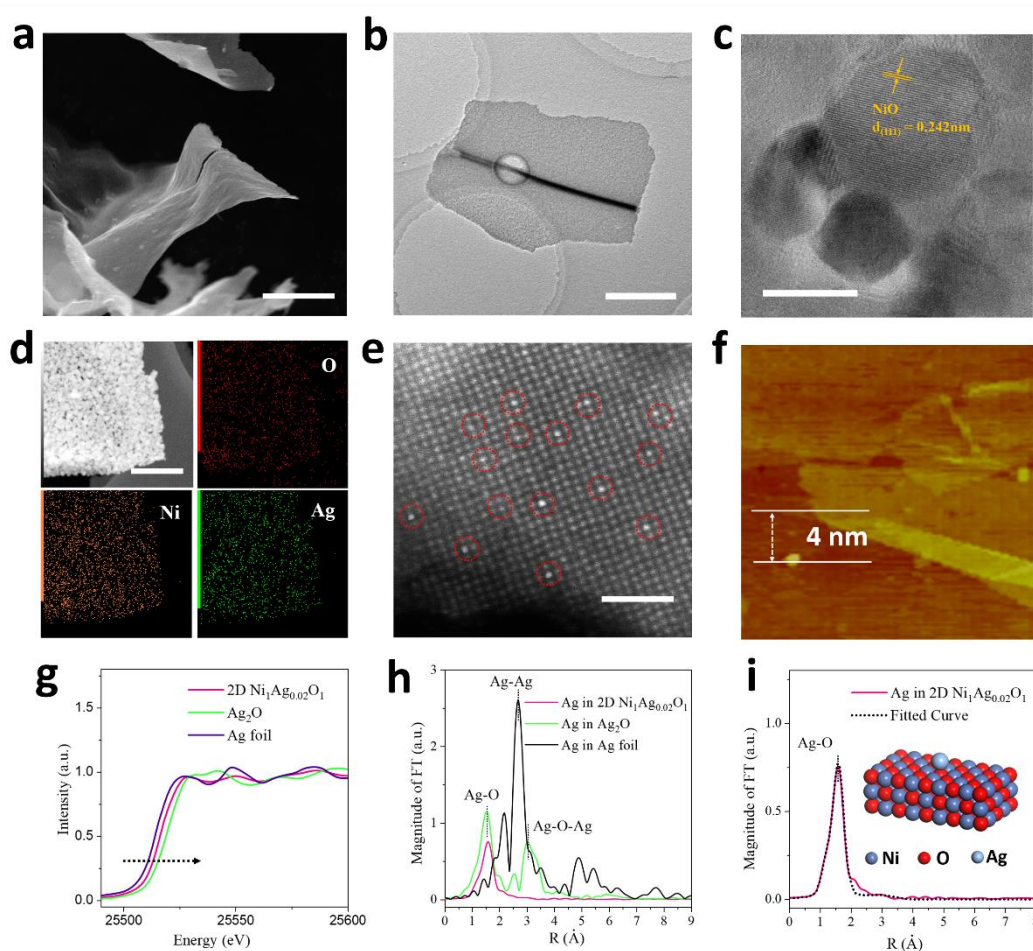


**Fig. 1** The characterization of 2D  $\text{Ni}_1\text{Ag}_{0.02}\text{O}_1$ . **a** SEM image, **b** TEM image, **c** HRTEM image of 2D  $\text{Ni}_1\text{Ag}_{0.02}\text{O}_1$ . **d** STEM image and EDS mapping of 2D  $\text{Ni}_1\text{Ag}_{0.02}\text{O}_1$ . **e** HAADF-STEM image, **f** AFM image of 2D  $\text{Ni}_1\text{Ag}_{0.02}\text{O}_1$ . **g**, **h** XANES spectra and

FTEXAFS spectra at the Ag K-edge for 2D Ni<sub>1</sub>Ag<sub>0.02</sub>O<sub>1</sub>, Ag<sub>2</sub>O, and metallic Ag foil. **i** The FTEXAFS curves of the proposed 2D Ni<sub>1</sub>Ag<sub>0.02</sub>O<sub>1</sub> structure (black line) and the measured 2D Ni<sub>1</sub>Ag<sub>0.02</sub>O<sub>1</sub> (purple line). Inset is the proposed model of 2D Ni<sub>1</sub>Ag<sub>0.02</sub>O<sub>1</sub> architecture. The scale bars in **a, b, c, d, e** are 2 μm, 1 μm, 5 nm, 500 nm, 1 nm, respectively.

### **The RWGS performance of 2D Ni<sub>1</sub>Ag<sub>0.02</sub>O<sub>1</sub>**

Fig. 2a shows the RWGS performance of 2D Ni<sub>1</sub>Ag<sub>0.02</sub>O<sub>1</sub>, Ni nanosheets (defined as Ni, Supplementary Fig. 4-6, synthesis details can be found in the Methods sections), Ag nanoparticles (defined as Ag, Supplementary Fig. 7-10). For a fair comparison, we set the activation temperature at a point where the RWGS CO production rate is higher than 1 mmol g<sup>-1</sup> h<sup>-1</sup>. The RWGS activation temperature of 2D Ni<sub>1</sub>Ag<sub>0.02</sub>O<sub>1</sub>, Ni was 150 °C, 275 °C, respectively, and Ag remained inactive throughout the entire reaction temperature range (Fig. 2a). Further, the CO production rate of 2D Ni<sub>1</sub>Ag<sub>0.02</sub>O<sub>1</sub> reached 1434 mmol g<sup>-1</sup> h<sup>-1</sup> at 300 °C with 96.7% CO selectivity (Supplementary Fig. 11), 10.11% CO<sub>2</sub> conversion efficiency (Supplementary Fig. 12), exhibiting higher activity and selectivity in comparison with Ni (93.1 mmol g<sup>-1</sup> h<sup>-1</sup> of CO production rate and 90% CO selectivity at 300 °C, Supplementary Fig. 13). Fig. 2b and Supplementary Table 2 list the RWGS CO production rate of 2D Ni<sub>1</sub>Ag<sub>0.02</sub>O<sub>1</sub> and advanced catalysts at different temperatures. The CO production rate of 2D Ni<sub>1</sub>Ag<sub>0.02</sub>O<sub>1</sub> at 300 °C, 250 °C is 1434, 418.95 mmol g<sup>-1</sup> h<sup>-1</sup>, respectively, not only totally outperformed the best catalysts at corresponding temperatures (619.2 mmol g<sup>-1</sup> h<sup>-1</sup> at 300 °C, 277.2 mmol g<sup>-1</sup> h<sup>-1</sup> at



250 °C),<sup>26</sup> but also exceeded the catalysts working at higher temperature (350-430 °C, 434.7 mmol g<sup>-1</sup> h<sup>-1</sup> at 350 °C).<sup>22</sup> The 2D Ni<sub>1</sub>Ag<sub>0.02</sub>O<sub>1</sub> also showed a robust CO production rate of ~870 mmol g<sup>-1</sup> h<sup>-1</sup> in a continuous 76-hour RWGS test at 275 °C (Fig. 2c), verifying the excellent stability of 2D Ni<sub>1</sub>Ag<sub>0.02</sub>O<sub>1</sub>. The specific surface area of 2D Ni<sub>1</sub>Ag<sub>0.02</sub>O<sub>1</sub> was 31.5 m<sup>2</sup> g<sup>-1</sup> h<sup>-1</sup> (Supplementary Fig. 14), ~1.7 times of Ni (17.4 m<sup>2</sup> g<sup>-1</sup>, Supplementary Fig. 15). It indicates that the excellent RWGS activity of 2D Ni<sub>1</sub>Ag<sub>0.02</sub>O<sub>1</sub> mainly comes from high intrinsic activity of active sites. Fig. 2d shows that the apparent activation energy (E<sub>a</sub>) for 2D Ni<sub>1</sub>Ag<sub>0.02</sub>O<sub>1</sub> was around 7.55 kJ mol<sup>-1</sup>, which was 1/8 of Ni (~58.66 kJ mol<sup>-1</sup>), implying the great catalytic activity of 2D Ni<sub>1</sub>Ag<sub>0.02</sub>O<sub>1</sub>.

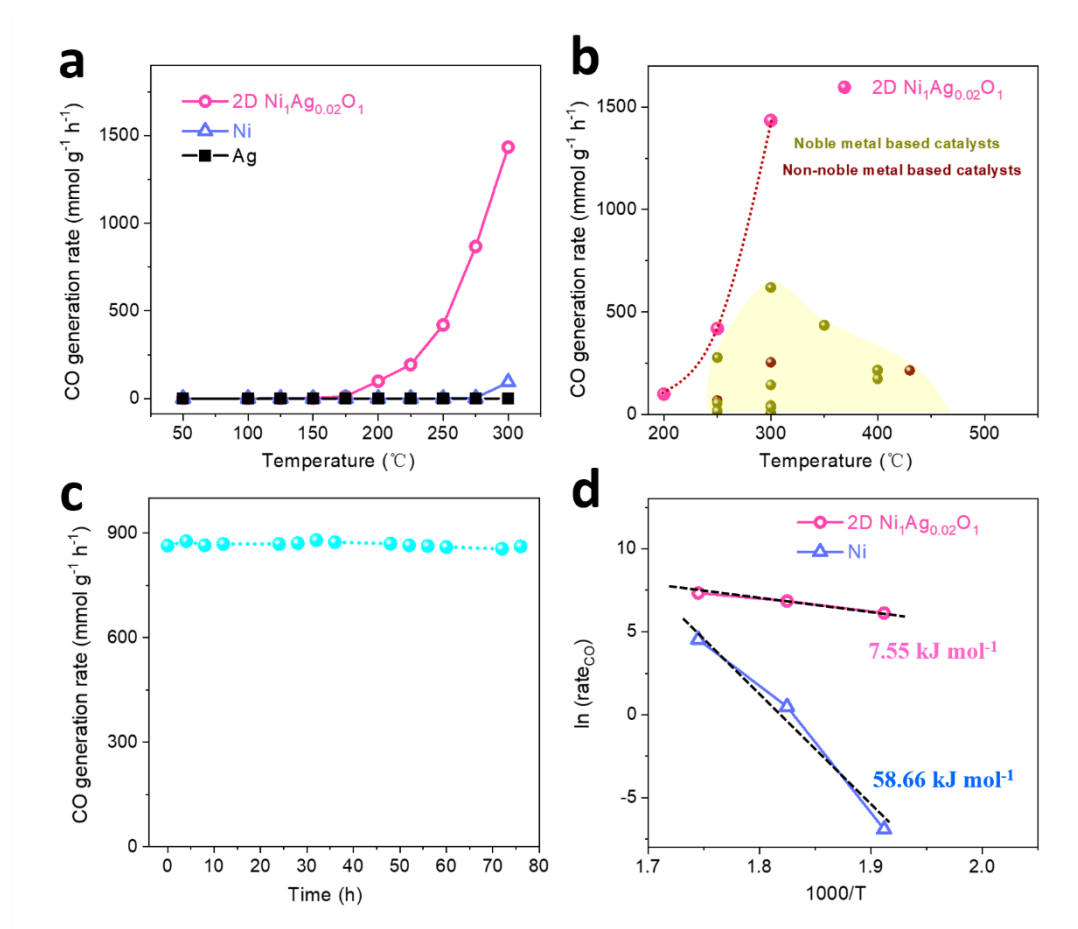


**Fig. 2** RWGS performance and mechanism of 2D Ni<sub>1</sub>Ag<sub>0.02</sub>O<sub>1</sub>. **a** The CO produced rate

of thermocatalytic RWGS over 2D Ni<sub>1</sub>Ag<sub>0.02</sub>O<sub>1</sub>, Ni, Ag. **b** The RWGS CO production rate of 2D Ni<sub>1</sub>Ag<sub>0.02</sub>O<sub>1</sub> and other advanced catalysts at different temperatures: Pt-MoO<sub>x</sub>/Mo<sub>2</sub>N (619.2 mmol g<sup>-1</sup> h<sup>-1</sup> at 300 °C),<sup>26</sup> Cu/Mo<sub>2</sub>C (253.6 mmol g<sup>-1</sup> h<sup>-1</sup> at 300 °C),<sup>35</sup> Fe-Pt/CeO<sub>2</sub> (142.9 mmol g<sup>-1</sup> h<sup>-1</sup> at 300 °C),<sup>22</sup> Pt/CeO<sub>2</sub> (43.2 mmol g<sup>-1</sup> h<sup>-1</sup> at 300 °C),<sup>36</sup> Na-Rh/ZrO<sub>2</sub> (37.4 mmol g<sup>-1</sup> h<sup>-1</sup> at 300 °C),<sup>23</sup> PtCo/TiO<sub>2</sub> (34.1 mmol g<sup>-1</sup> h<sup>-1</sup> at 300 °C),<sup>37</sup> Ru@MoO<sub>3-x</sub> (7.5 mmol g<sup>-1</sup> h<sup>-1</sup> at 300 °C),<sup>24</sup> Rh-In<sub>2</sub>O<sub>3-x</sub>(OH)<sub>y</sub> (2.4 mmol g<sup>-1</sup> h<sup>-1</sup> at 300 °C),<sup>38</sup> Pt-MoO<sub>x</sub>/Mo<sub>2</sub>N (277.2 mmol g<sup>-1</sup> h<sup>-1</sup> at 250 °C),<sup>26</sup> Co<sub>2</sub>C (68.04 mmol g<sup>-1</sup> h<sup>-1</sup> at 250 °C),<sup>39</sup> Fe-Pt/CeO<sub>2</sub> (54.48 mmol g<sup>-1</sup> h<sup>-1</sup> at 250 °C),<sup>22</sup> Ru-Mo-O<sub>x</sub> (18.75 mmol g<sup>-1</sup> h<sup>-1</sup> at 250 °C),<sup>40</sup> 2D-Mo<sub>2</sub>C (17.91 mmol g<sup>-1</sup> h<sup>-1</sup> at 250 °C),<sup>41</sup> Fe-Pt/CeO<sub>2</sub> (434.7 mmol g<sup>-1</sup> h<sup>-1</sup> at 350 °C),<sup>22</sup> Pd/TiO<sub>2</sub> (216 mmol g<sup>-1</sup> h<sup>-1</sup> at 400 °C),<sup>25</sup> Pt/CeO<sub>2</sub> (172.8 mmol g<sup>-1</sup> h<sup>-1</sup> at 400 °C),<sup>36</sup> 2D-Mo<sub>2</sub>C (214.3 mmol g<sup>-1</sup> h<sup>-1</sup> at 430 °C).<sup>41</sup> **c** The stability test of 2D Ni<sub>1</sub>Ag<sub>0.02</sub>O<sub>1</sub> for RWGS at 275 °C for 76 hours. The RWGS test condition in **a**, **b**, **c** is: Catalyst's amount = 5 mg, CO<sub>2</sub> flow rate = 30 mL min<sup>-1</sup>, H<sub>2</sub> flow rate = 30 mL min<sup>-1</sup>. **d** Apparent activation energy (E<sub>a</sub>) of 2D Ni<sub>1</sub>Ag<sub>0.02</sub>O<sub>1</sub>, Ni. The RWGS test condition of 2D Ni<sub>1</sub>Ag<sub>0.02</sub>O<sub>1</sub> in **d** is: Catalyst's amount = 2 mg, CO<sub>2</sub> flow rate = 30 mL min<sup>-1</sup>, H<sub>2</sub> flow rate = 30 mL min<sup>-1</sup>.

### Asymmetric sites activated RWGS

The mechanism of RWGS over 2D Ni<sub>1</sub>Ag<sub>0.02</sub>O<sub>1</sub> was investigated by Spin-polarized density functional theory (DFT).<sup>42</sup> Ag single atom bonded on NiO(200) plane was used to represent 2D Ni<sub>1</sub>Ag<sub>0.02</sub>O<sub>1</sub> and Ni(111) plane was used as the reference sample (Supplementary Fig. 16). And, *In-situ* DRIFTS spectroscopy was applied to identify the

intermediates to infer reaction pathways (Fig. 3a). For the adsorbed CO<sub>2</sub>, 2D Ni<sub>1</sub>Ag<sub>0.02</sub>O<sub>1</sub> showed the main peak at ~1597 cm<sup>-1</sup>, faint peaks at 1338 cm<sup>-1</sup>, 1238 cm<sup>-1</sup>, assigned to bridged CO<sub>2</sub> (b-CO<sub>3</sub>\*), monodentate carbonate (m-CO<sub>3</sub>\*), HCO<sub>3</sub>\*, respectively.<sup>43</sup> Whereas, Ni only showed the monodentate carbonate adsorption (Supplementary Fig. 17). Based on the adsorption results, we did the DFT calculation. For 2D Ni<sub>1</sub>Ag<sub>0.02</sub>O<sub>1</sub>, the Bader charge of Ag and Ni in 2D Ni<sub>1</sub>Ag<sub>0.02</sub>O<sub>1</sub> was +1.18 and +0.12 |e|, respectively. It made Ni in 2D Ni<sub>1</sub>Ag<sub>0.02</sub>O<sub>1</sub> tend to adsorb electron rich oxygen ion of CO<sub>2</sub> and Ag single atom have strong interaction with electron deficient carbon ion in CO<sub>2</sub> (Supplementary Fig. 16). The asymmetric adsorption of CO<sub>2</sub> in 2D Ni<sub>1</sub>Ag<sub>0.02</sub>O<sub>1</sub> made C=O bond extend to 1.38 Å, in comparison with the 1.2 Å of C=O length in CO<sub>2</sub> adsorbed on Ni(111), and this elongated C=O bond was easily activated.<sup>44</sup> In comparison, the CO<sub>2</sub> was adsorbed on Ni(111) by Ni-C bond (Supplementary Fig. 16). At 150 °C of reaction temperature, the intermediate of COOH\* (1750 cm<sup>-1</sup>) appeared on 2D Ni<sub>1</sub>Ag<sub>0.02</sub>O<sub>1</sub>,<sup>45</sup> which is the key intermediate in the reduction of CO<sub>2</sub> to CO, and the peak intensity of COOH\* grows clearly with increasing reaction temperature (Fig. 3a). For the carboxyl route of RWGS shown in Fig. 3 b,c, the formation of the carboxyl group was the rate-determining step. The elongated O=C=O on 2D Ni<sub>1</sub>Ag<sub>0.02</sub>O<sub>1</sub> could break as O=C-O- to bond the H atom to form O=C-OH (1.03 eV for 2D Ni<sub>1</sub>Ag<sub>0.02</sub>O<sub>1</sub>, 1.36 eV for Ni, Fig. 3b,c).<sup>46</sup> Fig. 3 d,e also show the RWGS process via formate route and the rate-determining step was the C=O bond breaking of formate. Due to the elongated C=O of CO<sub>2</sub>, the C=O bond on 2D Ni<sub>1</sub>Ag<sub>0.02</sub>O<sub>1</sub> was easily split than that on Ni(111) (0.84 eV for 2D Ni<sub>1</sub>Ag<sub>0.02</sub>O<sub>1</sub>, 1.46 eV for Ni, Fig. 3d,e). These

results confirmed that 2D Ni<sub>1</sub>Ag<sub>0.02</sub>O<sub>1</sub> could activate CO<sub>2</sub> by the synergistic effect of Ag single atom and neighbored Ni site. In addition to the reaction energy barrier, we found that the desorption of CO was also the key for RWGS. In Ni(111), the CO was adsorbed by Ni site with 1.53 eV of desorption energy (Supplementary Fig. 18a, Fig. 3b).<sup>47 48</sup> Due to asymmetric adsorption of CO<sub>2</sub>, the CO was adsorbed on the Ag single atom of 2D Ni<sub>1</sub>Ag<sub>0.02</sub>O<sub>1</sub> as shown in Supplementary Fig. 18b with desorption energy of 0.44 eV (Fig. 3 b,d). Ag species had weak adsorption for CO intrinsically,<sup>49</sup> thus leading to the low adsorption barrier of CO.

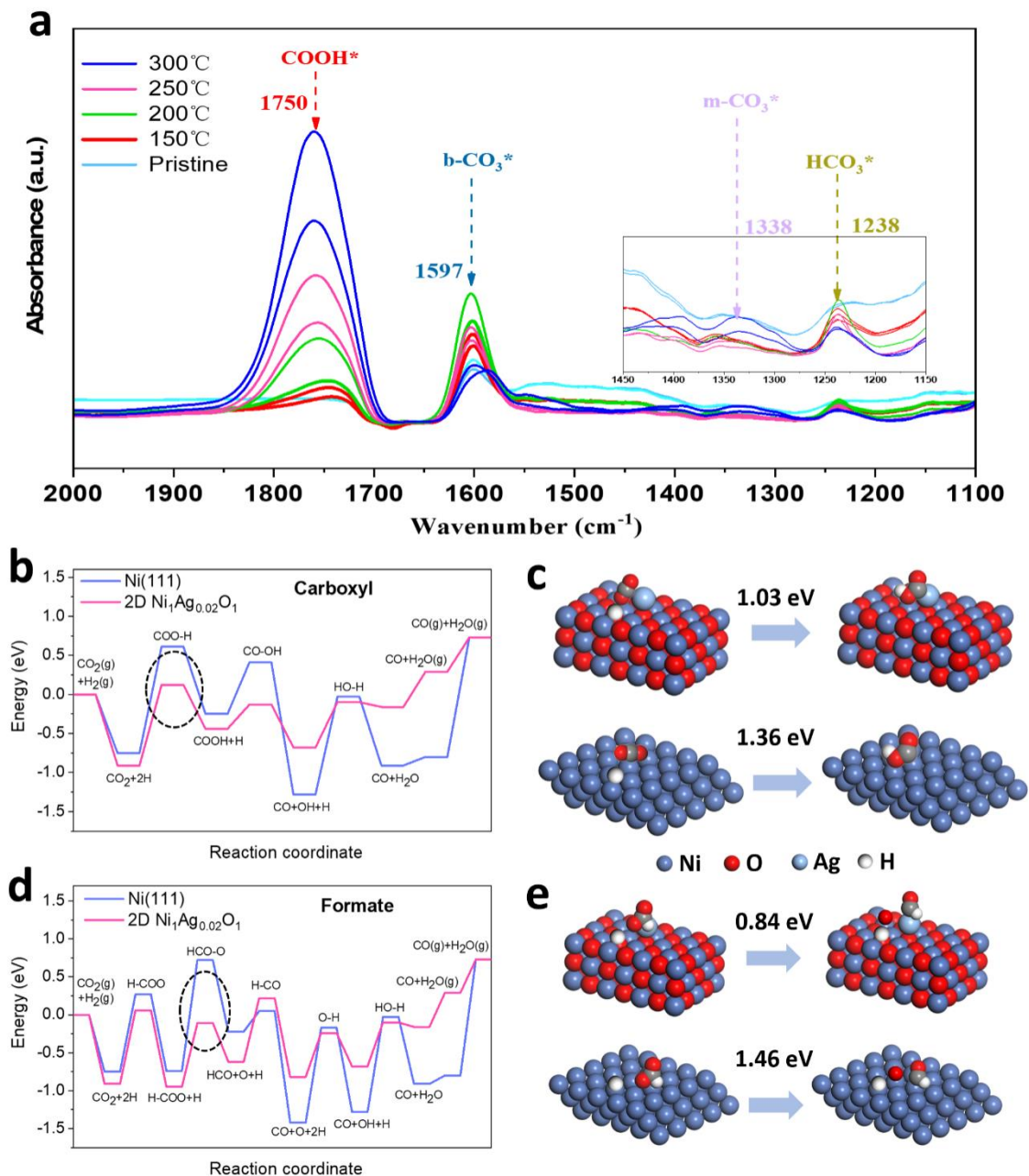


**Fig. 3** Ag-O-Ni synergistic effect and the reaction pathways for RWGS. **a** *In-situ* diffuse reflectance infrared Fourier transform spectra (DRIFTS) obtained for 2D  $\text{Ni}_1\text{Ag}_{0.02}\text{O}_1$  under RWGS operating condition. **b** Energy profiles of the RWGS via carboxyl route on Ni(111) and 2D  $\text{Ni}_1\text{Ag}_{0.02}\text{O}_1$ . **c** The configurations of rate-determining intermediates of the carboxyl route on Ni(111) and 2D  $\text{Ni}_1\text{Ag}_{0.02}\text{O}_1$ . **d** Energy profiles of the RWGS via formate route on Ni(111) and 2D  $\text{Ni}_1\text{Ag}_{0.02}\text{O}_1$ . **e** The configurations of rate-

determining intermediates of the formate route on Ni(111) and 2D Ni<sub>1</sub>Ag<sub>0.02</sub>O<sub>1</sub>.

### **Weak sunlight driven photothermal RWGS**

Due to the excellent low-temperature performance, 2D Ni<sub>1</sub>Ag<sub>0.02</sub>O<sub>1</sub> was applied for weak sunlight driven photothermal RWGS.<sup>17</sup> 2D Ni<sub>1</sub>Ag<sub>0.02</sub>O<sub>1</sub> was placed into the TiC/Cu based device for photothermal RWGS (Supplementary Fig. 19).<sup>50,51</sup> Just under 0.1 kW m<sup>-2</sup> intensity of sunlight (0.1 sun) irradiation, the photothermal RWGS was clearly onset with the catalyst's irradiation temperature reaching 125 °C (Fig. 4a). When the irradiated sunlight intensity increased to 0.5 sun and 1 sun, the catalyst's temperature was promoted to 264 °C and 350 °C, respectively. Meanwhile, the corresponding photothermal RWGS CO generation rate soared to 650 mmol g<sup>-1</sup> h<sup>-1</sup> and 1065 mmol g<sup>-1</sup> h<sup>-1</sup>, respectively. The CO selectivity of this system remained higher than 95% throughout the process (Supplementary Fig. 20). Fig. 4b and Supplementary Table 3 show the state of the art of photothermal RWGS. In previous reports, only when the light irradiation intensity exceeded 14 suns did CO production rate of photothermal RWGS surpass 100 mmol g<sup>-1</sup> h<sup>-1</sup>. Therefore, the 1 sun-driven photothermal RWGS CO production rate (1065 mmol g<sup>-1</sup> h<sup>-1</sup>) over 2D Ni<sub>1</sub>Ag<sub>0.02</sub>O<sub>1</sub> is not only the record performance under weak sunlight irradiation (1.01 mmol g<sup>-1</sup> h<sup>-1</sup> under 1 sun irradiation),<sup>52</sup> but also higher than the best value of advanced catalysts under concentrated sunlight irradiation (978.4 mmol g<sup>-1</sup> h<sup>-1</sup> under 28 suns irradiation).<sup>20</sup> Since the 2D Ni<sub>1</sub>Ag<sub>0.02</sub>O<sub>1</sub> can be scalably synthesized (Supplementary Fig. 21), we tested the performance of the photothermal system for RWGS. 30 g of granulated 2D Ni<sub>1</sub>Ag<sub>0.02</sub>O<sub>1</sub>

was placed in the TiC/Cu based device with 0.036 m<sup>2</sup> of sunlight irradiation area. When the sunlight density was 0.4 sun, 4.88 L h<sup>-1</sup> of CO generation rate appeared through the 2D Ni<sub>1</sub>Ag<sub>0.02</sub>O<sub>1</sub> loaded in the TiC/Cu based device (Fig. 4c). With increasing the light intensity to 1 sun, the CO generation rate increased to 30.2 L h<sup>-1</sup> (Fig. 4c). Based on the experimental data, the solar to chemical energy conversion efficiency (STC) of photothermal RWGS reached 39.1% under 1 sun irradiation (Fig. 4c). Therefore, the 2D Ni<sub>1</sub>Ag<sub>0.02</sub>O<sub>1</sub> made photothermal catalysis open a new pathway for achieving efficient weak solar driven CO<sub>2</sub> hydrogenation.

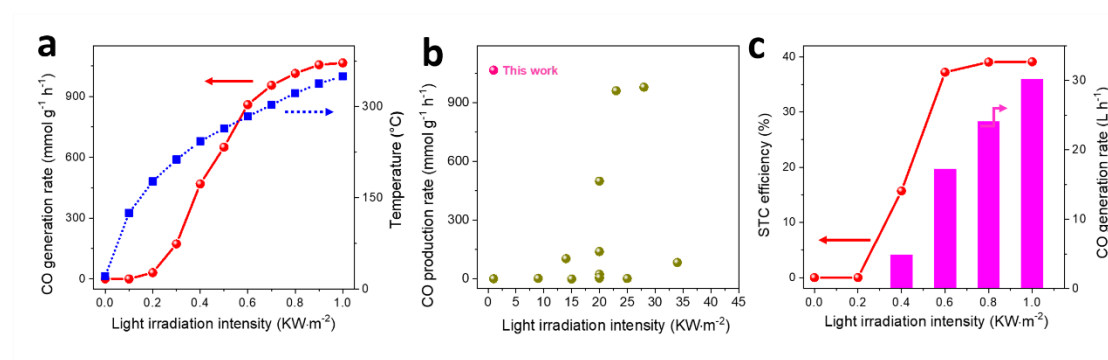


**Fig. 4** Weak sunlight driven photothermal RWGS. **a** The sunlight irradiation temperature and CO production rate of 2D Ni<sub>1</sub>Ag<sub>0.02</sub>O<sub>1</sub> combined with TiC/Cu based device. **b** The photothermal RWGS performance of reported state of the art of catalysts, e. g., BiO<sub>x</sub>/CeO<sub>2</sub> (1.01 mmol g<sup>-1</sup> h<sup>-1</sup>, 1 sun),<sup>52</sup> Ni@p-SiO<sub>2</sub> (978.4 mmol g<sup>-1</sup> h<sup>-1</sup>, 28 suns),<sup>20</sup> Ni<sub>12</sub>P<sub>5</sub>/SiO<sub>2</sub> (960 mmol g<sup>-1</sup> h<sup>-1</sup>, 23 suns),<sup>21</sup> Co-PS@SiO<sub>2</sub> (498.9 mmol g<sup>-1</sup> h<sup>-1</sup>, 20 suns),<sup>53</sup> CF-Cu<sub>2</sub>O (139.6 mmol g<sup>-1</sup> h<sup>-1</sup>, 20 suns),<sup>54</sup> 2D In<sub>2</sub>O<sub>3-x</sub> (103.21 mmol g<sup>-1</sup> h<sup>-1</sup>, 14 suns),<sup>55</sup> Ru/Mo<sub>2</sub>TiC<sub>2</sub> (84 mmol g<sup>-1</sup> h<sup>-1</sup>, 34 suns),<sup>56</sup> In<sub>2</sub>O<sub>3-x</sub> (23.8 mmol g<sup>-1</sup> h<sup>-1</sup>, 20 suns),<sup>57</sup> Bi<sub>x</sub>In<sub>2-x</sub>O<sub>3</sub> (8 mmol g<sup>-1</sup> h<sup>-1</sup>, 20 suns),<sup>58</sup> Pd@H<sub>y</sub>WO<sub>3-x</sub> (3 mmol g<sup>-1</sup> h<sup>-1</sup>, 20 suns),<sup>59</sup> Rh-In<sub>2</sub>O<sub>3-x</sub>(OH)<sub>y</sub> (2.4 mmol g<sup>-1</sup> h<sup>-1</sup>, 9 suns),<sup>38</sup> Pd/Nb<sub>2</sub>O<sub>5</sub> (1.8 mmol g<sup>-1</sup> h<sup>-1</sup>, 25 suns),<sup>60</sup>

Pd@SiNS ( $0.01 \text{ mmol g}^{-1} \text{ h}^{-1}$ , 15 suns).<sup>61</sup> The photothermal RWGS test condition in **a**, **b** is: catalyst's amount = 10 mg,  $\text{CO}_2$  flow rate =  $30 \text{ mL min}^{-1}$ ,  $\text{H}_2$  flow rate =  $30 \text{ mL min}^{-1}$ . **c** The CO production rate and STC efficiency of scalable photothermal RWGS. The photothermal RWGS test condition in **c** is: catalyst's amount = 30 g,  $\text{CO}_2$  flow rate =  $200 \text{ L h}^{-1}$ ,  $\text{H}_2$  flow rate =  $200 \text{ L h}^{-1}$ .

### **The application on outdoor artificial photosynthesis**

To realize the application of artificial photosynthesis, artificial photosynthesis system should have the characteristics of outdoor sunlight driven operation, large working area and high utilization rate of raw materials. As shown in Fig. 5a, an outdoor artificial photosynthesis system with  $103 \text{ m}^2$  scale was built by using photovoltaic-electrocatalysis ( $94 \text{ m}^2$  of irradiation area) to split water ( $2\text{H}_2\text{O} \rightarrow 2\text{H}_2 + \text{O}_2$ )<sup>62</sup> and using 2D  $\text{Ni}_1\text{Ag}_{0.02}\text{O}_1$  assisted photothermal catalysis ( $9 \text{ m}^2$  of irradiation area) to hydrogenate  $\text{CO}_2$  ( $\text{CO}_2 + \text{H}_2 \rightarrow \text{CO} + \text{H}_2\text{O}$ ).<sup>45,63,64</sup> In this system, the hydrogen generated from photovoltaic water electrolysis<sup>65</sup> was directly injected into the photothermal system for  $\text{CO}_2$  hydrogenation driven by sunlight.<sup>18,57,66</sup> On April 5, 2023, an outdoor artificial photosynthetic system for CO production was tested in Baoding City, Hebei Province, China, with an ambient temperature ranging from 7 to 19 °C during the daytime. The sunlight irradiation area of the system was  $103 \text{ m}^2$ , and 2 kg of 2D  $\text{Ni}_1\text{Ag}_{0.02}\text{O}_1$  was employed as the catalyst for photothermal RWGS. The outdoor sunlight intensity varied between 0.37 and  $0.76 \text{ kW m}^{-2}$  (Supplementary Fig. 22). As shown in Fig. 5b, when photovoltaic electrocatalysis generated  $\text{H}_2$  at 8:30 AM



(Supplementary Fig. 23), the photothermal system synchronously converted H<sub>2</sub> and CO<sub>2</sub> as CO, and the CO generation rate at 9:00 AM reached 1.83 m<sup>3</sup> h<sup>-1</sup>. On April 5, 2023, the CO generation rate in the outdoor artificial photosynthetic system increased to a peak value at 3.2 m<sup>3</sup> h<sup>-1</sup> at 12:00 PM, and then gradually decreased to 1.52 m<sup>3</sup> h<sup>-1</sup> at 16:00 PM. Although the solar intensity and ambient temperature are lower, the outdoor system STC for CO products can still be >16% throughout the operating period (Fig. 5c, detailed calculation seen in Methods). The daily total CO output of the system was ~18.70 m<sup>3</sup>. In the whole process, more than 90% of green H<sub>2</sub> was involved in the RWGS (Supplementary Fig. 24), which proved that the system can not only efficiently chemically store green H<sub>2</sub> generated by photovoltaic electrocatalysis, but also fix CO<sub>2</sub> on a large scale. Fig. 5d listed the STC values of reported advanced artificial photosynthetic systems with > 1 cm<sup>2</sup> of irradiation area. Firstly, the size of our outdoor artificial photosynthetic system is 103 m<sup>2</sup>, 15.8 times larger than the reported large-scale artificial photosynthesis (6.5 m<sup>2</sup>),<sup>15</sup> demonstrating its potential for mass production. Although used silicon solar cell, the STC of our outdoor demonstration for CO<sub>2</sub> reduction as CO is ~16.4%, which is not only 4.3 times higher than the STC of large-scale artificial photosynthesis (3.8%),<sup>15</sup> but also 1.3 times higher than that of reported advanced artificial photosynthetic systems (12.7%) by using triple-junction solar cells.<sup>16</sup> Consequently, the outdoor artificial photosynthetic system outperforms existing systems in terms of both scalability and conversion efficiency, making it a promising candidate for practical applications in CO<sub>2</sub> reduction and artificial photosynthesis.

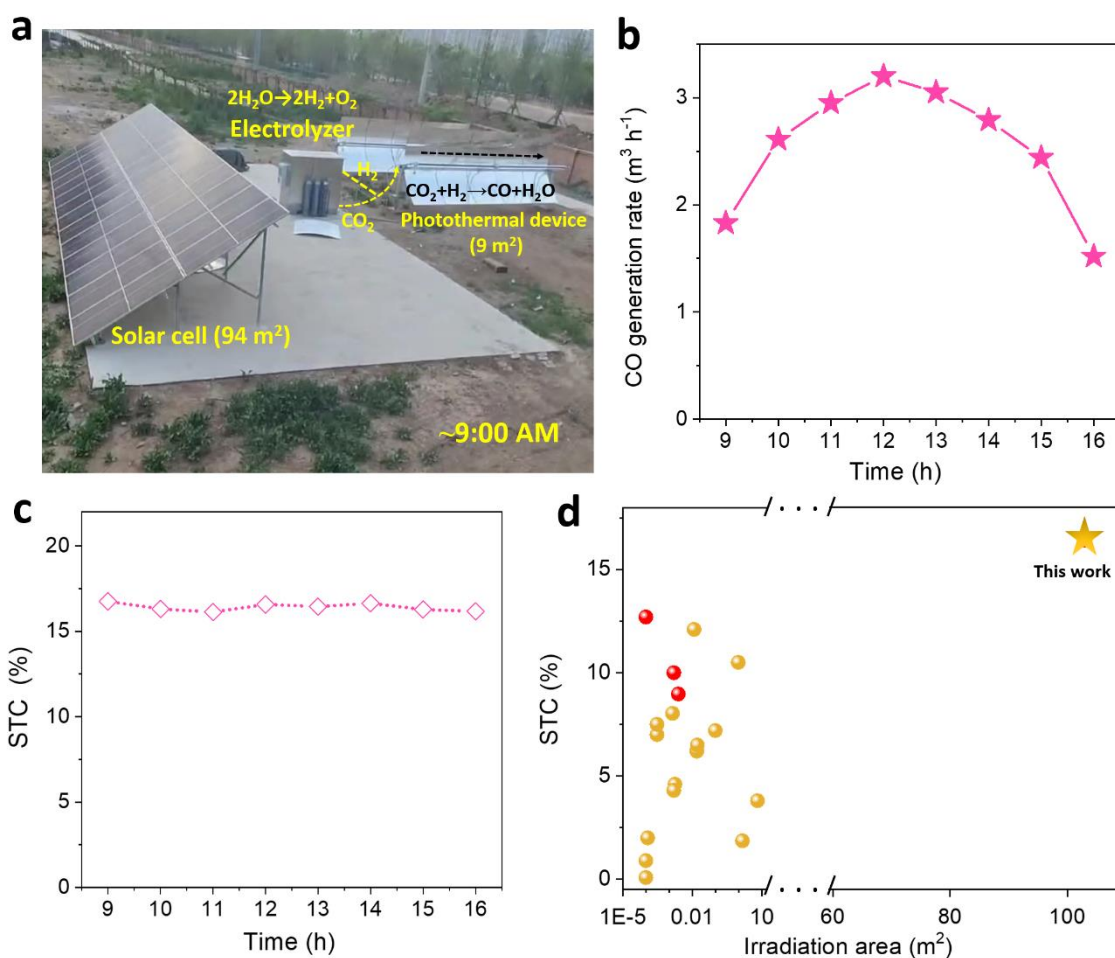


**Fig. 5** The outdoor performance of artificial photosynthetic system. **a** The photograph of new artificial photosynthetic demonstration in Hebei University. **b, c** The CO production rate and STC of new artificial photosynthetic demonstration under ambient sunlight irradiation, on April 05, 2023, in Baoding City, China. **d** Comparison of the solar driven CO<sub>2</sub> reduction systems of this work and the state of the art of artificial photosynthetic systems. The red spot represents that applied solar cell are triple-junction solar cell (28%-33% efficiency).<sup>67</sup> The STC and irradiation area of reported state of the art of artificial photosynthetic systems are as follows: (1.86%, 1.47 m<sup>2</sup>),<sup>68</sup> (3.8%, 6.5 m<sup>2</sup>),<sup>15</sup> (4.3%, 16 cm<sup>2</sup>),<sup>69</sup> (4.6%, 18 cm<sup>2</sup>),<sup>70</sup> (6.2%, 156 cm<sup>2</sup>),<sup>71</sup> (6.5%, 165

cm<sup>2</sup>),<sup>72</sup> (7.2%, 987 cm<sup>2</sup>),<sup>5</sup> (8.03%, 14 cm<sup>2</sup>),<sup>73</sup> (8.97%, 25 cm<sup>2</sup>),<sup>74</sup> (10.5%, 0.96 m<sup>2</sup>),<sup>6</sup>  
(12.1%, 120 cm<sup>2</sup>),<sup>75</sup> (2%, 1.18 cm<sup>2</sup>),<sup>76</sup> (7%, 3 cm<sup>2</sup>),<sup>77</sup> (10%, 16 cm<sup>2</sup>),<sup>78</sup> (7.5%, 3.198  
cm<sup>2</sup>),<sup>79</sup> (0.08%, 1 cm<sup>2</sup>),<sup>80</sup> (0.9%, 1 cm<sup>2</sup>),<sup>81</sup> (12.7%, 1 cm<sup>2</sup>).<sup>16</sup>

## Conclusion

In this work, a starch assisted templated method was developed to synthesize Ag single atoms supported on NiO nanosheets (2D Ni<sub>1</sub>Ag<sub>0.02</sub>O<sub>1</sub>). The resulting catalyst demonstrated excellent RWGS performance, with a CO production rate of 1434 mmol g<sup>-1</sup> h<sup>-1</sup> at 300 °C. *In-situ* DRIFTS and theoretical calculation indicated that the CO<sub>2</sub> was asymmetrically adsorbed on Ag-O-Ni sites of 2D Ni<sub>1</sub>Ag<sub>0.02</sub>O<sub>1</sub>, leading to the elongate C=O bond (1.38 Å). This enabled the active hydrogenation of CO<sub>2</sub> while also resulting in weak CO adsorption (0.44 eV). With the assistance of TiC/Cu based device, the 2D Ni<sub>1</sub>Ag<sub>0.02</sub>O<sub>1</sub> catalyst exhibited remarkable photothermal RWGS performance under 1-sun irradiation, with a CO production rate of 1065 mmol g<sup>-1</sup> h<sup>-1</sup>. Moreover, 94 m<sup>2</sup> of silicon solar cell was used to drive the electrolyzer for photovoltaic electrolytic water splitting as O<sub>2</sub> and H<sub>2</sub>, then, the generated H<sub>2</sub> and CO<sub>2</sub> were injected into the TiC/Cu based device (9 m<sup>2</sup>) loaded with 2D Ni<sub>1</sub>Ag<sub>0.02</sub>O<sub>1</sub> to carry out photothermal CO<sub>2</sub> hydrogenation. This system demonstrated a CO production of 18.70 m<sup>3</sup> per day and the solar to chemical energy conversion efficiency of >16% all day-time, under ambient solar irradiation. This work revealed that Ag single atom modification provided a new route to construct low-temperature CO<sub>2</sub> hydrogenation catalysts without platinum-group-metals. Based on the low-temperature CO<sub>2</sub> hydrogenation activity, 2D Ni<sub>1</sub>Ag<sub>0.02</sub>O<sub>1</sub> could drive ambient sunlight driven photothermal RWGS and new artificial photosynthesis to realize natural sunlight-driven carbon neutralization. This breakthrough has significant implications for the development of sustainable energy

solutions and environmental protection, offering a viable alternative to artificial photosynthesis and traditional catalysts.

## **Methods**

### **Chemicals for catalysts**

Commercial silver nitrate ( $\text{AgNO}_3$ ), nickel nitrate hydrate ( $\text{Ni}(\text{NO}_3)_2 \cdot 6\text{H}_2\text{O}$ ), water-soluble starch, Ag nanoparticles were bought from Sinopharm Co., Ltd. The chemicals were all used without any further treatment.

### **2D $\text{Ni}_1\text{Ag}_{0.02}\text{O}_1$**

Firstly, 10g water-soluble starch, 12 mg  $\text{AgNO}_3$  and 972 mg  $\text{Ni}(\text{NO}_3)_2 \cdot 6\text{H}_2\text{O}$  were dissolved into 400 mL of water. After 0.5 hours of stirring, the uniform solution was dripped into liquid nitrogen to make it freeze into ice quickly and it was freeze-dried for 48 hours to remove  $\text{H}_2\text{O}$ . The dried product was calcined in a muffle furnace at  $425\text{ }^\circ\text{C}$  (heating rate  $1\text{ }^\circ\text{C min}^{-1}$ ) for 17 hours, and the obtained was named 2D  $\text{Ni}_1\text{Ag}_{0.02}\text{O}_1$ .

### **Ni**

Firstly, 10g water-soluble starch, 972 mg  $\text{Ni}(\text{NO}_3)_2 \cdot 6\text{H}_2\text{O}$  were dissolved into 400 mL of water. After 0.5 hours of stirring, the uniform solution was dripped into liquid nitrogen to make it freeze into ice quickly and it was freeze-dried for 48 hours to remove  $\text{H}_2\text{O}$ . The dried product was calcined in a muffle furnace at  $425\text{ }^\circ\text{C}$  (heating rate  $1\text{ }^\circ\text{C min}^{-1}$ ) for 17 hours, and then the annealed sample was reduced by  $\text{H}_2$  at  $400\text{ }^\circ\text{C}$  for 5 hours to achieve the sample.

## Photothermal RWGS

The photothermal RWGS was tested as follows: 10 mg of 2D Ni<sub>1</sub>Ag<sub>0.02</sub>O<sub>1</sub> was loaded into TiC/Cu based device (0.036 m<sup>2</sup>), and irradiated by a light source (DL-3000). In this test, the flow of feed gas was the mixture of 30 mL min<sup>-1</sup> of CO<sub>2</sub> and 30 mL min<sup>-1</sup> of H<sub>2</sub>. The reaction products were tested by gas chromatography (GC) 7890A equipped with FID and TCD detectors.

For the scalable test, the amount of 2D Ni<sub>1</sub>Ag<sub>0.02</sub>O<sub>1</sub> was increased to 30 g, the flow of feed gas was the mixture of 200 L h<sup>-1</sup> of CO<sub>2</sub> and 200 L h<sup>-1</sup> of H<sub>2</sub>.

## Enthalpy change energy of chemicals

The enthalpy change energy of CO<sub>2</sub> (g), CO (g), H<sub>2</sub> (g), O<sub>2</sub> (g), H<sub>2</sub>O (g), H<sub>2</sub>O (l) was -393.505, -110.541, 0, 0, -241.818, -285.830 kJ mol<sup>-1</sup>, respectively.

The (g) and (l) indicated the gas state and liquid state, respectively.

## Solar to chemical energy conversion efficiency (STC) of photothermal RWGS

The STC of photothermal RWGS demonstration was calculated as follows:

$$\text{STC} = (\Delta H \cdot \varepsilon / 24.5) / (I \cdot S \cdot 3600) \quad (1)$$

$\Delta H$  was the reaction Enthalpy change energy (CO<sub>2</sub> (g) + H<sub>2</sub> (g) → CO (g) + H<sub>2</sub>O (g)), RWGS,  $\Delta H = 41.15$  kJ mol<sup>-1</sup>),  $\varepsilon$  (L h<sup>-1</sup>) was the CO generation amount per hour detected by a flowmeter,  $I$  was the light intensity (kW m<sup>-2</sup>),  $S$  was the irradiated area of demonstration (0.036 m<sup>2</sup>). The  $\varepsilon$  irradiated by 0.4 sun, 0.6 sun, 0.8 sun, 1 sun was 4.88 L h<sup>-1</sup>, 17.22 L h<sup>-1</sup>, 24.10 L h<sup>-1</sup>, 30.20 L h<sup>-1</sup>, respectively, corresponding to 15.7%, 37.2%, 39.0%, 39.1% of STC, severally.

## Outdoor artificial photosynthetic system

The outdoor artificial photosynthetic system consisted of two components. One component was the photovoltaic electrolysis system, in which the solar cell (TSM-DE19) with 94 m<sup>2</sup> of solar irradiation area was used to power electrolytic reactor. The mixture of 30 kg KOH and 100 L deionized water was used as the electrolyte. The other component was the photothermal system, in which a TiC/Cu based photothermal device was provided by Hebei scientist research experimental and equipment trade Co., Ltd. with the size of 4 cm in diameter and 6 m inlength, equipped with a reflector of 6 m inlength and 1.5 m in width. For the production of CO, the catalyst used in TiC/Cu based photothermal device was 2 kg 2D Ni<sub>1</sub>Ag<sub>0.02</sub>O<sub>1</sub>. For CO production in photothermal system, the CO<sub>2</sub>/H<sub>2</sub> ratio was 12. The data were collected by FID and TCD.

### **The STC of outdoor artificial photosynthetic system**

The STC of the outdoor artificial photosynthetic system for converting CO<sub>2</sub> into CO was calculated as follows:

$$STC = (\Delta H * \epsilon) / (I * S * 3.6 * 22.4) \quad (2)$$

$\Delta H$  was the reaction Enthalpy change energy ( $H_2O(l) + CO_2(g) \rightarrow CO(g) + 1/2 O_2(g) + H_2O(g)$ ,  $\Delta H = 326.9754 \text{ kJ mol}^{-1}$ ),  $\epsilon$  (m<sup>3</sup>) was the CO generation amount per hour detected by a flowmeter,  $I$  was the outdoor solar intensity (kW m<sup>-2</sup>), and the  $I$  at 9:00 AM, 10:00 AM, 11:00 AM, 12:00 AM, 13:00 PM, 14:00 PM, 15:00 PM, 16:00 PM was 0.43 kW m<sup>-2</sup>, 0.63 kW m<sup>-2</sup>, 0.72 kW m<sup>-2</sup>, 0.76 kW m<sup>-2</sup>, 0.73 kW m<sup>-2</sup>, 0.66 kW m<sup>-2</sup>, 0.59 kW m<sup>-2</sup>, 0.37 kW m<sup>-2</sup>, respectively.  $S$  was the total irradiated area of 103 m<sup>2</sup>. The  $\epsilon$  at 9:00 AM, 10:00 AM, 11:00 AM, 12:00 AM, 13:00 PM, 14:00 PM, 15:00 PM, 16:00 PM

was 1.83 m<sup>3</sup> h<sup>-1</sup>, 2.61 m<sup>3</sup> h<sup>-1</sup>, 2.95 m<sup>3</sup> h<sup>-1</sup>, 3.20 m<sup>3</sup> h<sup>-1</sup>, 3.05 m<sup>3</sup> h<sup>-1</sup>, 2.79 m<sup>3</sup> h<sup>-1</sup>, 2.44 m<sup>3</sup> h<sup>-1</sup>, 1.52 m<sup>3</sup> h<sup>-1</sup>, respectively, corresponding to 16.75%, 16.30%, 16.13%, 16.57%, 16.44%, 16.64%, 16.28%, 16.17% of STC, severally.

## Data availability

The data generated in this study are provided in the main text and Supplementary information. Extra data are available from the corresponding author upon reasonable request. Source data are provided with this paper.

## References

- 1 Zhou, P. *et al.* Solar-to-hydrogen efficiency of more than 9% in photocatalytic water splitting. *Nature* **613**, 66-70, (2023).
- 2 Yang, Y. *et al.* Operando studies reveal active Cu nanograins for CO<sub>2</sub> electroreduction. *Nature* **614**, 262-269, (2023).
- 3 Li, X. G. *et al.* Isolated FeN<sub>4</sub> Sites for Efficient Electrocatalytic CO<sub>2</sub> Reduction. *Adv. Sci.* **7**, 6, (2020).
- 4 Mehla, S. *et al.* Porous crystalline frameworks for thermocatalytic CO<sub>2</sub> reduction: an emerging paradigm. *Energy Environ. Sci.* **14**, 34, (2021).
- 5 Kato, N. *et al.* A large-sized cell for solar-driven CO<sub>2</sub> conversion with a solar-to-formate conversion efficiency of 7.2%. *Joule* **5**, 687-705, (2021).
- 6 Kato, N. *et al.* Solar Fuel Production from CO<sub>2</sub> Using a 1 m-Square-Sized Reactor with a Solar-to-Formate Conversion Efficiency of 10.5%. *ACS Sust. Chem. Eng.* **9**, 16031-16037, (2021).
- 7 Xu, Y. *et al.* Low coordination number copper catalysts for electrochemical CO<sub>2</sub> methanation in a membrane electrode assembly. *Nat. Commun.* **12**, 2932-2932, (2021).
- 8 Devasia, D., Wilson, A. J., Heo, J., Mohan, V. & Jain, P. K. A rich catalog of C-C bonded species formed in CO<sub>2</sub> reduction on a plasmonic photocatalyst. *Nat. Commun.* **12**, 2612-2612, (2021).
- 9 Tang, C., Gong, P., Xiao, T. & Sun, Z. Direct electrosynthesis of 52% concentrated CO on silver's twin boundary. *Nat. Commun.* **12**, 2139, (2021).



- 10 Li, F. W. *et al.* Molecular tuning of CO<sub>2</sub>-to-ethylene conversion. *Nature* **577**, 509-513, (2020).
- 11 Nam, D. H. *et al.* Molecular enhancement of heterogeneous CO<sub>2</sub> reduction. *Nat. Mater.* **19**, 266-276, (2020).
- 12 Ma, W. C. *et al.* Electrocatalytic reduction of CO<sub>2</sub> to ethylene and ethanol through hydrogen-assisted C-C coupling over fluorine-modified copper. *Nat. Catal.* **3**, 478-487, (2020).
- 13 Ma, B. *et al.* Efficient Visible-Light-Driven CO<sub>2</sub> Reduction by a Cobalt Molecular Catalyst Covalently Linked to Mesoporous Carbon Nitride. *J. Am. Chem. Soc.* **142**, 6188-6195, (2020).
- 14 Qiu, X.-F., Zhu, H.-L., Huang, J.-R., Liao, P.-Q. & Chen, X.-M. Highly Selective CO<sub>2</sub> Electroreduction to C<sub>2</sub>H<sub>4</sub> Using a Metal-Organic Framework with Dual Active Sites. *J. Am. Chem. Soc.* **143**, 7242-7246, (2021).
- 15 Schäppi, R. *et al.* Drop-in fuels from sunlight and air. *Nature*, **601**, 63-68, (2022).
- 16 Jiang, K. *et al.* Transition-Metal Single Atoms in a Graphene Shell as Active Centers for Highly Efficient Artificial Photosynthesis. *Chem* **3**, 950-960, (2017).
- 17 Lv, C. *et al.* Nanostructured Materials for Photothermal Carbon Dioxide Hydrogenation: Regulating Solar Utilization and Catalytic Performance. *ACS Nano* **17**, 1725-1738, (2023).
- 18 Li, Y. *et al.* Selective light absorber-assisted single nickel atom catalysts for ambient sunlight-driven CO<sub>2</sub> methanation. *Nat. Commun.* **10**, 2359, (2019).
- 19 Li, Y. *et al.* A new artificial photosynthetic system coupling photovoltaic electrocatalysis with solar heating catalysis. *Natl. Sci. Open* **2**: 20230033, (2023).
- 20 Cai, M. *et al.* Greenhouse-inspired supra-photothermal CO<sub>2</sub> catalysis. *Nat. Energy* **6**, 807-814, (2021).
- 21 Xu, Y.-F. *et al.* High-performance light-driven heterogeneous CO<sub>2</sub> catalysis with near-unity selectivity on metal phosphides. *Nat. Commun.* **11**, 5149, (2020).
- 22 Wang, H. *et al.* Synergistic Interactions of Neighboring Platinum and Iron Atoms Enhance Reverse Water-Gas Shift Reaction Performance. *J. Am. Chem. Soc.* **145**, 2264-2270, (2023).
- 23 Li, S. *et al.* Tuning the CO<sub>2</sub> Hydrogenation Selectivity of Rhodium Single-Atom Catalysts on Zirconium Dioxide with Alkali Ions. *Angew. Chem. Int. Edit.* **135**, e202218167 (2023).
- 24 Xin, H. *et al.* Overturning CO<sub>2</sub> Hydrogenation Selectivity with High Activity via Reaction-Induced Strong Metal-Support Interactions. *J. Am. Chem. Soc.* **144**, 4874-4882, (2022).
- 25 Nelson, N. C., Chen, L., Meira, D., Kovarik, L. & Szanyi, J. In Situ Dispersion of Palladium on TiO<sub>2</sub> During Reverse Water-Gas Shift Reaction: Formation of Atomically Dispersed Palladium. *Angew. Chem. Int. Edit.* **59**, 17657-17663, (2020).
- 26 Liu, H.-X. *et al.* Ptn-Ov synergistic sites on MoO<sub>x</sub>/γ-Mo<sub>2</sub>N heterostructure for low-temperature reverse water-gas shift reaction. *Nat. Commun.* **13**, 5800 (2022).

- 27 Zhu, M. *et al.* Vacancy engineering of the nickel-based catalysts for enhanced CO<sub>2</sub> methanation. *Appl. Catal. B-Environ.* **282**, 119561, (2021).
- 28 Zhu, P., Jing, L., Zuo, S. & Zhou, R. Preferential oxidation properties of CO in excess hydrogen over CuO-CeO<sub>2</sub> catalyst prepared by hydrothermal method. *Appl. Surf. Sci.* **255**, 2903-2909 (2008).
- 29 Li, Y. *et al.* Low Temperature Thermal and Solar Heating Carbon-Free Hydrogen Production from Ammonia Using Nickel Single Atom Catalysts. *Adv. Energy Mater.* **12**, 2202459, (2022).
- 30 Zhang, N. *et al.* Silver Single-Atom Catalyst for Efficient Electrochemical CO<sub>2</sub> Reduction Synthesized from Thermal Transformation and Surface Reconstruction. *Angew. Chem. Int. Edit.* **60**, 6170-6176, (2021).
- 31 Hu, C. *et al.* Orthogonal Charge Transfer by Precise Positioning of Silver Single Atoms and Clusters on Carbon Nitride for Efficient Piezocatalytic Pure Water Splitting. *Angew. Chem. Int. Edit.* **61**, e202212397, (2022).
- 32 Herzog, A. *et al.* Operando Investigation of Ag-Decorated Cu<sub>2</sub>O Nanocube Catalysts with Enhanced CO<sub>2</sub> Electroreduction toward Liquid Products. *Angew. Chem. Int. Edit.* **60**, 7426-7435, (2021).
- 33 Zhang, H., Itoi, T., Konishi, T. & Izumi, Y. Dual Photocatalytic Roles of Light: Charge Separation at the Band Gap and Heat via Localized Surface Plasmon Resonance To Convert CO<sub>2</sub> into CO over Silver–Zirconium Oxide. *J. Am. Chem. Soc.* **141**, 6292-6301, (2019).
- 34 Zhang, Z. *et al.* “Two Ships in a Bottle” Design for Zn–Ag–O Catalyst Enabling Selective and Long-Lasting CO<sub>2</sub> Electroreduction. *J. Am. Chem. Soc.* **143**, 6855-6864, (2021).
- 35 Zhang, X. *et al.* Highly dispersed copper over β-Mo<sub>2</sub>C as an efficient and stable catalyst for the reverse water gas shift (RWGS) reaction. *ACS Catal.* **7**, 912-918 (2017).
- 36 Zhao, Z. *et al.* Atomically dispersed Pt/CeO<sub>2</sub> catalyst with superior CO selectivity in reverse water gas shift reaction. *Appl. Catal. B-Environ.* **291**, 120101, (2021).
- 37 Kattel, S. *et al.* CO<sub>2</sub> Hydrogenation over Oxide-Supported PtCo Catalysts: The Role of the Oxide Support in Determining the Product Selectivity. *Angew. Chem. Int. Edit.* **55**, 7968-7973, (2016).
- 38 Yan, T. *et al.* Polymorph selection towards photocatalytic gaseous CO<sub>2</sub> hydrogenation. *Nat. Commun.* **10**, 2521 (2019).
- 39 Zhang, S. *et al.* Morphological Modulation of Co<sub>2</sub>C by Surface-Adsorbed Species for Highly Effective Low-Temperature CO<sub>2</sub> Reduction. *ACS Catal.* **12**, 8544-8557, (2022).
- 40 Xin, H. *et al.* Overturning CO<sub>2</sub> Hydrogenation Selectivity with High Activity via Reaction-Induced Strong Metal–Support Interactions. *J. Am. Chem. Soc.* **144**, 4874-4882, (2022).
- 41 Zhou, H. *et al.* Two-dimensional molybdenum carbide 2D-Mo<sub>2</sub>C as a superior catalyst for CO<sub>2</sub> hydrogenation. *Nat. Commun.* **12**, 5510, (2021).
- 42 Lv, C. *et al.* Efficient hydrogen production via sunlight-driven thermal formic

- acid decomposition over a porous film of molybdenum carbide. *J. Mater. Chem. A* **9**, 22481-22488, (2021).
- 43 Mino, L., Spoto, G. & Ferrari, A. M. CO<sub>2</sub> Capture by TiO<sub>2</sub> Anatase Surfaces: A Combined DFT and FTIR Study. *J. Phys. Chem. C* **118**, 25016-25026, (2014).
- 44 Zhang, Y., Xia, B., Ran, J., Davey, K. & Qiao, S. Z. Atomic-Level Reactive Sites for Semiconductor-Based Photocatalytic CO<sub>2</sub> Reduction. *Adv. Energy Mater.* **10**, 1903879, (2020).
- 45 Tai, H., Nishikawa, K., Higuchi, Y., Mao, Z.-w. & Hirota, S. Cysteine SH and Glutamate COOH Contributions to [NiFe] Hydrogenase Proton Transfer Revealed by Highly Sensitive FTIR Spectroscopy. *Angew. Chem. Int. Edit.* **58**, 13285-13290, (2019).
- 46 Li, C. *et al.* Accelerating water dissociation at carbon supported nanoscale Ni/NiO heterojunction electrocatalysts for high-efficiency alkaline hydrogen evolution. *Nano Research*, 1-9, (2022).
- 47 Eichler, A. CO adsorption on Ni(111)-a density functional theory study. *Surf. Sci.* **526**, 332-340, (2003).
- 48 Nagarajan, V. & Chandiramouli, R. NiO nanocone as a CO sensor: DFT investigation. *Struct. Chem.* **25**, 1765-1771, (2014).
- 49 Sawabe, K. & Satsuma, A. Theoretical Study on Carbon Monoxide Adsorption on Unsupported and  $\gamma$ -Al<sub>2</sub>O<sub>3</sub>-Supported Silver Nanoparticles: Size, Shape, and Support Effects. *ACS Omega* **7**, 4405-4412, (2022).
- 50 Li, Y. *et al.* General heterostructure strategy of photothermal materials for scalable solar-heating hydrogen production without the consumption of artificial energy. *Nat. Commun.* **13**, 776, (2022).
- 51 Li, Y. *et al.* Cu-based high-entropy two-dimensional oxide as stable and active photothermal catalyst. *Nat. Commun.* **14**, 3171, (2023).
- 52 Kang, X. *et al.* Bismuth single atom supported CeO<sub>2</sub> nanosheets for oxidation resistant photothermal reverse water gas shift reaction. *Catal. Sci. Technol.* **12**, 5559-5564, (2022).
- 53 Feng, K. *et al.* Cobalt plasmonic superstructures enable almost 100% broadband photon efficient CO<sub>2</sub> photocatalysis. *Adv. Mater.* **32**, 2000014 (2020).
- 54 Wan, L. *et al.* Cu<sub>2</sub>O nanocubes with mixed oxidation-state facets for (photo)catalytic hydrogenation of carbon dioxide. *Nat. Catal.* **2**, 889-898 (2019).
- 55 Qi, Y. *et al.* Photoinduced Defect Engineering: Enhanced Photothermal Catalytic Performance of 2D Black In<sub>2</sub>O<sub>3-x</sub> Nanosheets with Bifunctional Oxygen Vacancies. *Adv. Mater.* **32**, 1903915, (2020).
- 56 Wu, Z. *et al.* Mo<sub>2</sub>TiC<sub>2</sub> MXene-Supported Ru Clusters for Efficient Photothermal Reverse Water-Gas Shift. *ACS Nano*, (2022).
- 57 Wang, L. *et al.* Black indium oxide a photothermal CO<sub>2</sub> hydrogenation catalyst. *Nat. Commun.* **11**, 2432, (2020).
- 58 Yan, T. *et al.* Bismuth atom tailoring of indium oxide surface frustrated Lewis pairs boosts heterogeneous CO<sub>2</sub> photocatalytic hydrogenation. *Nat. Commun.* **11**, 6095 (2020).
- 59 Zhang, L. *et al.* Decontamination of U(VI) on graphene oxide/Al<sub>2</sub>O<sub>3</sub> composites

- investigated by XRD, FT-IR and XPS techniques. *Environ. Pollut.* **248**, 332-338, (2019).
- 60 Jia, J. *et al.* Visible and Near-Infrared Photothermal Catalyzed Hydrogenation of Gaseous CO<sub>2</sub> over Nanostructured Pd@Nb<sub>2</sub>O<sub>5</sub>. *Adv. Sci.* **3**, 1600189, (2016).
- 61 Qian, C. *et al.* Catalytic CO<sub>2</sub> reduction by palladium-decorated silicon-hydride nanosheets. *Nat. Catal.* **2**, 46-54, (2019).
- 62 Xu, Y. Q., Zhang, W. F., Li, Y. G., Lu, P. F. & Wu, Z. S. A general bimetal-ion adsorption strategy to prepare nickel single atom catalysts anchored on graphene for efficient oxygen evolution reaction. *J. Energy Chem.* **43**, 52-57, (2020).
- 63 Ju, T. *et al.* Dicarboxylation of alkenes, allenes and (hetero)arenes with CO<sub>2</sub> via visible-light photoredox catalysis. *Nat. Catal.* **4**, 304-311, (2021).
- 64 Salvatore, D. A. *et al.* Designing anion exchange membranes for CO<sub>2</sub> electrolyzers. *Nat. Energy* **6**, 339-348, (2021).
- 65 Jia, J. Y. *et al.* Solar water splitting by photovoltaic-electrolysis with a solar-to-hydrogen efficiency over 30%. *Nat. Commun.* **7**, 6, (2016).
- 66 Chen, Y. *et al.* Cooperative catalysis coupling photo-/photothermal effect to drive Sabatier reaction with unprecedented conversion and selectivity. *Joule* **5**, 3235-3251, (2021).
- 67 Schreier, M. *et al.* Solar conversion of CO<sub>2</sub> to CO using Earth-abundant electrocatalysts prepared by atomic layer modification of CuO. *Nat. Energy* **2**, 17087, (2017).
- 68 White, J. L., Herb, J. T., Kaczur, J. J., Majsztik, P. W. & Bocarsly, A. B. Photons to formate: Efficient electrochemical solar energy conversion via reduction of carbon dioxide. *Journal of CO<sub>2</sub> Utilization* **7**, 1-5, (2014).
- 69 Urbain, F. *et al.* A prototype reactor for highly selective solar-driven CO<sub>2</sub> reduction to synthesis gas using nanosized earth-abundant catalysts and silicon photovoltaics. *Energy Environ. Sci.* **10**, 2256-2266, (2017).
- 70 Asadi, M. *et al.* Nanostructured transition metal dichalcogenide electrocatalysts for CO<sub>2</sub> reduction in ionic liquid. *Science* **353**, 467-470, (2016).
- 71 Lourenço, A. C., Reis-Machado, A. S., Fortunato, E., Martins, R. & Mendes, M. J. Sunlight-driven CO<sub>2</sub>-to-fuel conversion: Exploring thermal and electrical coupling between photovoltaic and electrochemical systems for optimum solar-methane production. *Mater. Today Energy* **17**, 100425, (2020).
- 72 Sriramagiri, G. M. *et al.* Toward a Practical Solar-Driven CO<sub>2</sub> Flow Cell Electrolyzer: Design and Optimization. *ACS Sust. Chem. Eng.* **5**, 10959-10966, (2017).
- 73 Chae, S. Y. *et al.* A perspective on practical solar to carbon monoxide production devices with economic evaluation. *Sust. Energy Fuel.* **4**, 199-212, (2020).
- 74 Esmaeilrad, M. *et al.* Oxygen Functionalized Copper Nanoparticles for Solar-Driven Conversion of Carbon Dioxide to Methane. *ACS Nano* **14**, 2099-2108, (2020).
- 75 Lee, W. H. *et al.* W@Ag dendrites as efficient and durable electrocatalyst for solar-to-CO conversion using scalable photovoltaic-electrochemical system.

- Appl. Catal. B-Environ.* **297**, 120427, (2021).
- 76 Thijs, B. *et al.* Demonstration of a three compartment solar electrolyser with gas phase cathode producing formic acid from CO<sub>2</sub> and water using Earth abundant metals. *Frontiers in Chemical Engineering* **4**, 1028811, (2022).
- 77 Choi, S. Y., Kim, T. W., Jeong, H. W. & Park, H. Photoelectrochemical behaviors and photocatalytic activities of mixed CuO and CuFeO<sub>2</sub> films with Ti and Ni underlayers for CO<sub>2</sub> conversion. *Appl. Catal. A-General* **654**, 119071, (2023).
- 78 Prajapati, A. *et al.* CO<sub>2</sub>-free high-purity ethylene from electroreduction of CO<sub>2</sub> with 4% solar-to-ethylene and 10% solar-to-carbon efficiencies. *Cell Reports Physical Science* **3**, 101053, (2022).
- 79 Gurudayal *et al.* Efficient solar-driven electrochemical CO<sub>2</sub> reduction to hydrocarbons and oxygenates. *Energy Environ. Sci.* **10**, 2222-2230, (2017).
- 80 Lee, S., Jang, G. Y., Kim, J. K. & Park, J. H. Solar-harvesting lead halide perovskite for artificial photosynthesis. *J. Energy Chem.* **62**, 11-26, (2021).
- 81 Deng, K. *et al.* A high-pressure artificial photosynthetic device: pumping carbon dioxide as well as achieving selectivity. *J. Mater. Chem. A* **9**, 3961-3967, (2021).

## Acknowledgements

This work is supported by the Natural Science Foundation of Hebei Province (Grant Nos. B2022201090, B2021201074, B2021201034, F2021203097), Interdisciplinary Research Program of Natural Science of Hebei University (Grant Nos. 521100311, DXK202109), Hebei University (050001-521100302025, 050001-513300201004), the Knowledge Innovation Program of the Chinese Academy of Sciences. Thank you for the TEM technical support provided by the Microanalysis Center, College of Physics Science and Technology, Hebei University.

## Author contributions

Y. L., Q. M. conceived the project and contributed to the design of the experiments and analysis of the data. Q. W. and D. Y. performed the catalysts preparation and characterizations. H. W., B. L., and J. W. performed the photothermal devices' characterizations. F. M., X. S., L. G. conducted the SEM and TEM examinations. S. W. provided the optical advice. Y. L. and Q. M. wrote the paper. All the authors discussed the results and commented on the manuscript.

## Competing interests

The Authors declare no competing interests.

## Additional information

**Supplementary Information** accompanies this paper.

**Correspondence** and requests for materials should be addressed to Yaguang Li or Qingbo Meng.

**Reprints and permission** information is available online.

**Publisher's note:** Springer Nature remains neutral with regard to jurisdictional claims in published maps and institutional affiliations.